Extremely sensitive detection of NO$_2$ employing off-axis integrated cavity output spectroscopy coupled with multiple-line integrated absorption spectroscopy

Gottipaty N. Rao* and Andreas Karpf

Department of Physics, Adelphi University, Garden City, New York 11530, USA

*Corresponding author: Rao@adelphi.edu

We report on the development of a new sensor for NO$_2$ with ultrahigh sensitivity of detection. This has been accomplished by combining off-axis integrated cavity output spectroscopy (OA-ICOS) (which can provide large path lengths of the order of several kilometers in a small volume cell) with multiple-line integrated absorption spectroscopy (MLIAS) (where we integrate the absorption spectra over a large number of rotational–vibrational transitions of the molecular species to further improve the sensitivity). Employing an external cavity quantum cascade laser operating in the 1601–1670 cm^{-1} range and a high-finesse optical cavity, the absorption spectra of NO$_2$ over 100 transitions in the R band have been recorded. From the observed linear relationship between the integrated absorption versus concentration of NO$_2$ and the standard deviation of the integrated absorption signal, we report an effective sensitivity of detection of approximately 28 ppt (parts in 10^{12}) for NO$_2$. To the best of our knowledge, this is among the most sensitive levels of detection of NO$_2$ to date.   © 2011 Optical Society of America

OCIS codes: 010.1120, 010.0280, 140.5965.

1. Introduction

The real-time detection of trace gases in the parts-per-billion (ppb, parts in 10^9) and parts-per-trillion (ppt, parts in 10^{12}) levels is of great interest in a wide range of fields, including environmental science and air quality control {e.g., for compliance with Environmental Protection Agency (EPA) regulations [1,2]}, defense and homeland security (e.g., for the detection of trace amounts of explosive compounds [3]), medical diagnostics [4], detecting trace impurities in the semiconductor industry [5], and optimizing combustion processes and minimizing pollution emissions [6], to name a few. Laser-based techniques are well suited for trace gas detection because of their ability to provide real-time monitoring capabilities with a high degree of sensitivity and selectivity. In particular, quantum cascade lasers (QCLs) (which emit in the mid-infrared region covering 4–24 μm) are especially attractive for this task, because they provide access to the fundamental rotational–vibrational transitions of molecular species [7–9]. QCLs have been used to detect several trace gasses, including CO, CO$_2$, NO, NO$_2$, NH$_3$, CH$_4$, and N$_2$O [7–9], as well as explosive compounds such as TNT [3]. A reliable NO$_2$ monitor capable of high sensitivity and selectivity would be valuable for monitoring atmospheric air quality (to meet EPA air quality standards [1,2] and monitor the formation of photochemical smog, tropospheric ozone, and automobile and industrial emissions) as well as for the real-time study of the complex photochemical reactions that the NO$_x$ gases undergo in the atmosphere.

A variety of spectroscopic techniques have been developed for detection, each having its own merits and limitations. The spectroscopic techniques that are commonly employed include absorption spectroscopy

using long path-length absorption cells such as multipass and Herriott cells; optical cavity methods (cavity ring-down spectroscopy, off-axis integrated cavity output spectroscopy); photoacoustic and quartz-enhanced photoacoustic spectroscopy; and Faraday rotation spectroscopy. Various data processing and analysis procedures have been applied, such as frequency modulated spectroscopy techniques to improve the signal-to-noise ratio and multiple-line integrated absorption spectroscopy to improve the sensitivity of detection. The current status of much of this work was presented in the recent review articles by Tittel *et al.* [8], Curl et al. [9], and Rao and Karpf [10].

External cavity tunable QCLs are quite compact, operate at room temperature, have long operating lifetimes, require low power levels for operation, provide reasonably high output powers with a narrow laser linewidth, and can be operated over a wide tuning range (hundreds of wavenumbers), which make them well suited for trace gas monitoring applications in real time. Trace gas detection using laser absorption spectroscopy is based on recording the change in intensity of laser radiation as it passes through a region containing the sample of interest. In this technique the laser is tuned across specific molecular transitions of interest, the spectra are synchronously added and averaged, and either compared with molecular cross-section data or secondary calibration procedures are employed to obtain the concentrations. In order to detect very low concentration species in the ppb level or lower, one would employ multipass cells to increase the path length and improve the sensitivity of detection. Using multipass optical cells, one can reach path lengths in the hundreds of meters range; however, the volume of these cells is large (typically about 1 liter). The main difficulty with multipass cells is that they are bulky, involve careful cavity adjustments, and are sensitive to vibrations, which are potential limitations for field applications. Fabry–Perot optical cavities provide long path lengths of the order of several kilometers in a small effective volume [11–14]. In this technique, the laser is coupled to a high finesse optical cavity (formed by highly reflective, low-loss dielectric mirrors) so that a large amount of light energy builds up within the cavity. In cavity ring-down spectroscopy (CRDS), one interrupts the laser beam and measures the exponential decay of the light exiting the cavity (cavity ring-down time) with and without the gas sample. While CRDS offers high sensitivity of detection and provides an absolute value of the absorption coefficient (i.e., no need for secondary calibration procedures), it is susceptible to vibrations and requires stringent cavity resonance conditions. An additional limitation to CRDS is its dependence on high-speed detection electronics due to the short time scale of most cavity ring-down (CRD) decays. In the present work, we employ off-axis integrated cavity output spectroscopy (OA-ICOS), which typically provides path lengths of the order of several kilom-

eters. In this technique, we align the laser in an off-axis configuration with the high finesse optical cavity to generate a high density of transverse cavity modes. We dither the cavity length and simultaneously modulate the laser to randomize the modes and record usable spectra. The OA-ICOS technique is particularly attractive for trace gas sensors, because the system does not involve the complex cavity locking mechanisms or stringent resonance conditions necessary in CRDS experiments, is less sensitive to vibrations, and does not require high-speed electronics. The off-axis arrangement allows a range of laser input directions compared to a single normal incidence condition that is necessary for the cavity resonance condition. When using external cavity QCLs, OA-ICOS offers an additional advantage over CRDS in that it is less susceptible to problems related to optical feedback and the associated laser output instabilities [15]. As discussed in our recent paper, optical feedback [15] is a major problem in mid-infrared laser-based work since optical isolators are not commercially available in this region.

In the present work, we coupled OA-ICOS with multiple-line integrated absorption spectroscopy (MLIAS) [16,17] recently proposed by us. In this technique, instead of monitoring a single absorption peak as is traditionally done, we scan the laser over a large number of rotational–vibrational transitions and take the sum of the areas of all the absorption peaks (after subtracting the background) for sensitivity measurements. Employing this method, the sensitivity of detection can be significantly improved.

2. OA-ICOS

In cavity enhanced absorption spectroscopy techniques, one employs a tunable laser and a high finesse optical cavity and observes the cavity output while tuning the laser over the wavelength range of interest [11,12]. These techniques are known in the literature as integrated cavity output spectroscopy (ICOS) [11] and cavity-enhanced absorption spectroscopy [12]. In OA-ICOS [13], the laser is aligned in an off-axis configuration to create an extremely dense population of optical modes within the cavity that approaches a continuum. The continuum of modes enables us to average the cavity transmission spectrum more effectively, resulting in a significant improvement in the sensitivity of detection [18].

In CRDS the optical cavity is carefully aligned such that the TEM_{00} mode is dominant. This is accomplished by aligning the laser beam so that it coincides with the cavity axis. As one tunes the laser and the resonance condition is satisfied, the cavity output is characterized by sharp spikes separated by the free spectral range (FSR) of the cavity; the width of the spike depends on the cavity finesse. In the case of OA-ICOS, the laser beam is incident at a small angle with respect to the cavity axis, resulting in a large number of cavity modes including $TEM_{00}, TEM_{01}, TEM_{02}, \ldots TEM_{mn}$. The cavity transmission spectra thus consists of a large number of

spikes at frequencies corresponding to the different modes. The intensity of the transmitted peaks depends on the overlap between the laser and the cavity modes. As we go to higher modes (TEM_{mn}), the cavity FSR gets $(n + m)$ times smaller compared to the TEM_{00} mode, and the density of modes increases [19]. In OA-ICOS, we carefully misalign the cavity such that the density of cavity modes becomes higher and approaches a continuum of modes. At the same time we make sure that the beam undergoes a large number of reflections in the cavity thus ensuring a long path length before the reentrant condition is reached. Ideally, when a continuum of modes is achieved, the intensity of the light exiting when a laser is tuned should not depend on the laser's frequency. Thus, if an absorbing gas species is present in the cavity, the drops in the intensity of light exiting the cavity represent the absorption spectra specific to the species. The signal-to-noise ratio of a single scan spectrum is often not satisfactory because the cavity modes are not completely random, resulting in mode noise. Therefore, dithering one of the mirrors of the cavity and/or modulating the laser frequency and averaging over multiple scans effectively randomizes the mode structure and thus significantly improves the signal-to-noise ratio. This results in transmission spectra that correspond to the characteristic absorption lines of the gas species [19,20].

A variety of cavity configurations can result in stable off-axis path lengths through a cavity. For a two mirror cavity with spherical mirrors, the experimental arrangement must satisfy the stability condition [21]:

$$0 \leq \left(1 - \frac{L}{R_1}\right)\left(1 - \frac{L}{R_2}\right) < 1, \tag{1}$$

where L is the mirror spacing (50 cm). We used two spherical mirrors with identical radii of curvatures ($R_1 = R_2 = 1\,\text{m}$) and reflection coefficients $R = 0.9998$.

For a cw laser, under steady-state conditions, the intracavity power may be written as [13]

$$I = \frac{I_0 C_p T}{2(1 - R)}, \tag{2}$$

where I_0 is the incident laser intensity, C_p is the cavity coupling parameter (it has a value between 0 and 1 and can reach 1 for a well-matched TEM_{00} mode), R is the reflectivity of the mirrors (assumed constant for both the mirrors), and T is the transmission coefficient of the mirrors (again assumed constant for both the mirrors).

When a weakly absorbing medium is placed between the mirrors, R is replaced with an effective reflectivity R' [13]:

$$R' = Re^{-\alpha(\nu)L}, \tag{3}$$

where $\alpha(\nu)L$ is the absorbance of the medium in the cavity. Equations (2) and (3) show that the absorbance information is contained in the steady-state intracavity intensity and thus can be measured via the light exiting the cavity. The change in the steady-state output of the cavity due to the presence of the absorbing species in the cavity may be expressed in the form [13]

$$\frac{\Delta I}{I_0} = \frac{\text{GA}}{1 + \text{GA}}, \tag{4}$$

where $A = 1 - e^{-\alpha(\nu)L}$ and $G = R/(1 - R)$. Therefore, for weak absorption, the cavity provides a large linear gain in the absorption signal. For trace gas species, $\text{GA} \ll 1$. Thus GA can be neglected in the denominator of Eq. (4) and may be rewritten in the form

$$\frac{I_0(\nu) - I(\nu)}{I_0(\nu)} = \frac{\alpha(\nu)L}{(1 - R)}. \tag{5}$$

The relative change in the laser intensity is directly proportional to the absorption coefficient and hence the number density of the trace species. The presence of the $(1 - R)$ term in the denominator gives a large enhancement in the signal compared to single-pass absorption. We recorded the ICOS steady-state cavity output intensity as a function of the laser frequency as we tuned the laser.

3. MLIAS

As the laser is tuned across a transition, the transmitted laser intensity is a function of frequency ν given by Beer's law:

$$I(\nu) = I_0(\nu)e^{-\alpha(\nu)L}, \tag{6}$$

where I_0 is the incident laser intensity, L is the optical path length, and $\alpha(\nu)$ is the absorption coefficient at frequency ν [22]. In the low-concentration regime (where $\alpha(\nu)L \leq 0.05$) one can approximate Eq. (6) as

$$I(\nu) = I_0(\nu)[1 - \alpha(\nu)L]. \tag{7}$$

The sensitivity of a spectrometer is often determined by taking the ratio of the amplitudes of the absorption line to that of the noise level.

Using an absorption line's amplitude to detect a species, however, neglects the width of the line and as a result gives the same intensity for both broad and narrow lines with the same amplitude. For example, even though a sample of NO_2 at 600 mbars has 12 times more molecules than the same sample at 50 mbars, its absorption spectrum shows only about a 25% enhancement in peak absorption: The majority of additional absorption manifests itself in the broadening of the lines [16]. As a result, when dealing with broadened lines, a more accurate measure of the absorption intensity can be achieved by

using the area under the absorption curve instead of the amplitude. Assuming that $\alpha(\nu)L$ is small (as is typically the case with trace gas detection), the integrated absorption may be written as

$$S = \int \alpha(\nu)L\,d\nu. \tag{8}$$

For a single transition, the absorption coefficient $\alpha(\nu) = \sigma(\nu)N$ [where $\sigma(\nu)$ is the cross section and N is the concentration]. The cross section depends on the Einstein A coefficients of the levels and the statistical weight factors. The integral is to be carried out over Doppler and collisional broadened lineshape functions. Thus, the integrated absorption is proportional to the concentration N. While each of the absorption peaks is a complex function as detailed above, one can define an experimental parameter S_T, which is equal to the number density N_i multiplied by the sum of the areas under the different absorption peaks. Based on this, it has been shown that the sum of the areas of a set of absorption lines varies linearly with concentration, and conducting trace gas detection by integrating over multiple absorption lines can enhance the sensitivity of a detection by over 1 order of magnitude [16]. The sum of the areas of multiple absorption lines may be defined as the experimental parameter S_T and measured for different concentrations of the target species:

$$S_T = \sum_i \int \alpha_i(\nu)L\,d\nu. \tag{9}$$

Here $\alpha_i(\nu)$ is the absorption coefficient of the ith transition of the target species, and the summation is over all transitions within the selected tuning range of the detector. Using precalibrated reference mixtures of the desired gas, one can define an S_T versus a concentration curve that characterizes a particular experimental apparatus (e.g., this would take into account the optical path length L, the tuning range, and other equipment-related factors, as well as the Einstein A coefficients, the statistical weight factors, the Doppler, and the collisional broadened absorption lines). One can then identify unknown concentrations of the species by recording their S_T and identifying their corresponding concentrations on this chart.

This procedure enhances the sensitivity of detection in three ways. The first enhancement is due to the summing of the areas under many spectral lines (which boosts the magnitude of the recorded signal). The second enhancement is from the fact that the integration has the effect of averaging the random components of the noise. Because of the fact that these data are acquired in a single scan (which can take less than a second), this effective averaging of the noise occurs in a shorter time span than would be the case for averaging the signal by adding repeated fast scans. The sensitivity is further enhanced over standard laser absorption techniques in that

one is not limited to working in the low-pressure regime (i.e., there is no need to resolve the lines individually). This procedure is particularly valuable for molecules that have a large number of transitions grouped together.

4. Experimental Details

We carried out ICOS of NO_2 using a continuous wave QCL purchased from Daylight Solutions (Model TLS-CW-MHF). The QCL used an external cavity (comprising a diffraction grating aligned in a Littrow configuration) to provide a wide range of mode-hop free tuning (1604 to $1670\,cm^{-1}$) and a narrow linewidth ($\sim 0.001\,cm^{-1}$), which is well suited for spectroscopic measurements. The laser power varied as a function of tuning, with a minimum output power of $14\,mW$ at $1604\,cm^{-1}$, and a maximum of $21\,mW$ at $1640.4\,cm^{-1}$. The output power at $1656\,cm^{-1}$ (the frequency at which we conducted the present measurements) was $17\,mW$. The laser could be tuned using three different methods. Coarse tuning (over the entire range of the QCL) was accomplished using a stepper motor to rotate the diffraction grating. A piezoelectric transducer (PZT) allowed for fine tuning of the diffraction grating over a $2\,cm^{-1}$ range. Additionally, high-frequency tuning over a smaller $1\,cm^{-1}$ range was available via current modulation. In the reported work, the stepper motor was used to tune the laser to the desired spectral region, and a triangle wave from a Stanford Research Systems DS345 function generator was used to drive the PZT and tune the laser over a $2\,cm^{-1}$ range at a frequency of $3\,Hz$.

The experimental cell was constructed using components and mirrors purchased from Los Gatos Research. The cell was $50\,cm$ long, had mirrors with a radius of curvature of $1\,m$, and a reflectivity of 99.98% at $1650\,cm^{-1}$. The cell was connected to a vacuum system that allowed it to be loaded with different concentrations of the sample species (see Fig. 1).

Phase-sensitive detection was done using an IntraAction model AGM-402A6/11 acousto-optic modulator (AOM) to chop the QCL beam at a frequency of $5\,kHz$. Light exiting the experimental cell was focused onto a detector using an off-axis paraboloidal reflector. The signal was detected using a two-stage, TE-cooled, IR photovoltaic detector (PVI-2TE-8 manufactured by Vigo), which was operated in a room-temperature environment. The detector was optically immersed in a high refractive index, hyperhemispherical lens. The detector signal was fed to a lock-in amplifier (Stanford Research Systems SR830 DSP). The lock-in time constant was set to $3\,ms$. The signal from the lock-in was fed to a scaling amplifier (Stanford Research Systems SIM983) and then to a Tektronix DPO3034 digitizing oscilloscope. The oscilloscope output was fed to a PC via USB connection and recorded using Tektronix software.

The AOM chopping frequency for lock-in detection was selected such that the duration of each pulse was much longer than the ring-down time and thus did
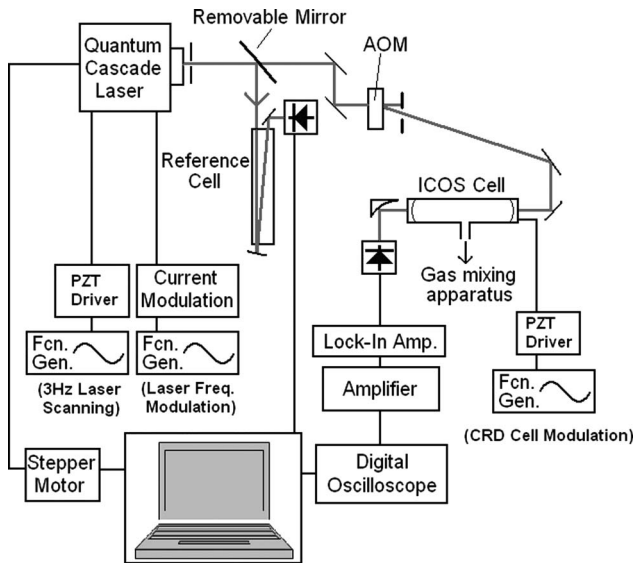
Fig. 1. Schematic of the experimental setup used for multiple-line integrated absorption spectroscopy employing ICOS for the trace detection of NO_2.

not interfere with the averaging of the cavity output for ICOS (i.e., in the absence of additional laser modulation, the pulse duration was selected to be long enough for the intracavity intensity to achieve the steady-state condition). To accomplish this, we first measured the ring-down time for the empty CRD cell by precisely aligning the cavity mirrors with the incoming QCL beam to form a standing wave. This resulted in a large energy buildup within the cavity. The input light was interrupted using the high-speed AOM chopper, and the exponential decay time of the light exiting the cavity (known as the ring-down time) was measured. For an empty cavity, the ring-down time depends on the reflectivity of the mirrors, and is given by

$$\tau_0 = \frac{L}{c(1-R)}, \tag{10}$$

where R is the mirror reflectivity, and L is the distance between the cavity's mirrors. The ring-down time for the CRD cell was measured to be $8.7 \pm 0.15\,\mu s$, which corresponded to the mirrors' stated reflectivity of 99.98%. The chopping frequency of 5 kHz was selected such that the duration of a pulse was over an order of magnitude longer than the ring-down time. The signal-to-noise ratio of the ICOS signal was tested for a variety of chopper frequencies between 1 and 20 kHz, with the optimal signal-to-noise ratio occurring at approximately 5 kHz.

The off-axis ICOS alignment did not result in a continuum mode structure (due to incomplete averaging of the cavity modes) and resulted in mode noise in the ICOS spectrum. Removal of the mode noise required further averaging by modulating both the laser frequency and the CRD cell length. The modulation frequencies were chosen such that the overlap time of the laser line with the cavity resonance (i.e.,

the time during which laser is coupled to the cavity) is insufficient for the cavity to reach the saturation resonance condition [11]. Using the linewidth of the Daylight Solutions QCL ($\Delta\nu \sim 40\,MHz$) and the FSR of the cavity ring-down cell (300 MHz), we calculated that modulating the laser at a frequency of 50 kHz would result in the laser being coupled to the cavity resonance for about one third of a ring-down time during each sweep. This was done by feeding a sine wave generated using a Stanford Research Systems model DS345 function generator into the current modulation input on the Daylight Solutions QCL head. The amplitude of the sine wave was chosen such that modulation of the laser line spanned one FSR of the CRD cell. The CRD cell length was modulated at a frequency of 300 Hz to further randomize the mode structure. This was accomplished by feeding a sine wave generated using another DS345 function generator to drive a Thorlabs model MDT693A piezo controller, which modulated a PZT connected to one of the mirrors in the CRD cell. The amplitude selected for the 300 Hz sine wave corresponded to modulating the CRD cell over one FSR. The signal-to-noise ratio was tested for a variety of laser modulation frequencies (between 10 kHz and 1 MHz) and a variety of CRD cell length modulation frequencies (between 10 and 500 Hz), with the optimal signal occurring for the values specified above.

The NO_2 mixtures were prepared by loading the experimental cell with a precalibrated mixture of NO_2 in zero air (a mix of 20.9% O_2 and 79.1% N_2). The precalibrated NO_2 mixture had a concentration of 5 parts in 10^6 (ppm) and was certified by Gasco Affiliates, LLC to $\pm10\%$ of the specified concentration. The concentrations used in the experiment were created by loading the cell with the 5 ppm mixture to a certain pressure and then adding zero air to increase the pressure to the desired final value (1000 mbars). For example, a 250 ppb concentration was generated by first loading the experimental cell with 50 ± 10 mbars of the precalibrated 5 ppm mix of NO_2 before additional zero air was added to reach a final pressure of 1000 ± 100 mbars. Because of limitations in the accuracy of our vacuum/mixing apparatus, the concentrations prepared are expected to be accurate to $\pm20\%$ (e.g., a 250 ppb concentration mixture is expected to contain between 200 and 300 ppb NO_2). The mixing apparatus was tested by generating several concentrations of NO_2 and comparing the recorded absorption spectra with simulated spectra generated using the HITRAN database [23] and the SPECTRA software developed by Mikhailenko et al. [24]. This confirmed that the mixtures were within the expected uncertainty.

Because of the limitations of our gas mixing apparatus, we were unable to reliably mix concentrations lower than about 100 ppb and thus simulated lower concentrations of NO_2 by conducting ICOS on a set of absorption lines whose multiple-line integrated absorption signal was 160 times weaker than the signal calculated for the strongest lines in the NO_2

R branch. The strongest lines in the R branch are located in the region between 1629.7 and 1631.7 cm^{-1} and comprise nearly 200 closely spaced transitions. The peak absorption in this region is due to two very closely spaced doublets located at approximately 1630.33 cm^{-1}; all four lines in these doublets are grouped within 0.003 cm^{-1} (the doublets are identified in Table 1). The lines used for the reported work were located between 1655.3 and 1657.3 cm^{-1} (see Fig. 2). They comprise approximately 115 closely spaced transitions, of which 34 could be said to contribute significantly to the spectrum (i.e., have transition strengths over 10% that of the strongest transition selected in the tuning range). Table 2 identifies the seven strongest doublets that contribute to absorption in the target region. The comparison of the strengths of the multiple-line integrated absorption signal from the strongest lines in the NO_2 R branch and the multiple-line integrated absorption signal from the weaker target region was carried out using simulated spectra generated using the HITRAN database [23] and the SPECTRA software [24]. By conducting ICOS on this weaker region, the effective concentrations of NO_2 of the mixtures used for the reported work were 11.9 ppb, 8.4 ppb, 6.3 ppb, 4.7 ppb, 3.1 ppb, and 1.6 ppb.

There were two main factors that needed to be considered for the selection of a region to carry out trace gas detection using MLIAS: (1) select a region with a strong dense spectrum, and (2) select a region free from interference due to other species. As mentioned above, the region used for this work (1655.3 to 1657.3 cm^{-1}) contained about 115 closely spaced lines and thus met the first requirement. A review of the component species present in the atmosphere and the species included in the HITRAN database [23,25] showed that only H_2O and NH_3 have transitions in this region that were potentially strong enough to cause interference. However, the effects of NH_3 in the reported work could be ignored due to the following reasons: (1) the expected concentration of NH_3 in ambient air (away from significant forest, industry, or farm sources) is in the 100 ppt–10 ppb range [26,27]; (2) purified NO_2 samples mixed with zero air used in the present experiments have insignificant amounts of NH_3; (3) the 1 m beam path from the laser to the experimental cell is 3 orders of magnitude shorter than the effective beam path in the CRD cell; (4) there are an order of magnitude fewer NH_3 transitions than NO_2 transitions in the target

Fig. 2. Simulated absorption spectrum of NO_2 (500 ppb concentration, 2000 m path length, pressure = 1000 mbars) covering the 1655.3 cm^{-1} to 1657.3 cm^{-1} region. Included in this figure is a "stick" spectrum identifying the individual transitions (and their relative strengths) that lead to the absorption spectrum. It should be noted that transitions that appear to be represented by dark bars are actually very closely spaced doublets.

region (between 1655.3 and 1657.3 cm^{-1}). We expect that the contributions to the observed signal from NH_3 are several orders of magnitude smaller than the signal from NO_2 and remain constant for all the NO_2 concentration measurements reported (since NH_3 contribution would be only from the ambient air outside the cell). Therefore, the effect of NH_3 in the present measurements can be neglected. It should be noted that the contributions from NH_3 can be neglected even if one were to monitor NO_2 in ambient air. In this case, one would investigate the absorption of the intense R-band transitions, the intensity of which are over an order of magnitude larger than the most prominent transitions of NH_3 in that region, and the number of NO_2 transitions are over a magnitude larger than the number of NH_3 transitions in the same region.

The strength of the water lines, however, necessitated that we select a region in which they did not significantly interfere with recording NO_2 spectra. Figure 3 shows a simulated spectrum illustrating

Table 1. Spectral Line Parameters from HITRAN [23] for the Major NO_2 Doublets That Are Responsible for the Peak Absorption in the R Branch

Central Frequency of Doublet (cm^{-1})	Upper State (ν_1 ν_3 ν_3)-(N' K_a' K_c')						Lower State (ν_1 ν_3 ν_3)-(N'' K_a'' K_c'')					
1630.326	(0	0	1)-(17	1	16)	(0	0	0)-(16	1	15)		
1630.328	(0	0	1)-(17	0	17)	(0	0	0)-(16	0	16)		

Table 2. Spectral Line Parameters from HITRAN [23] for the Strongest NO_2 Doublets in the Target Region (between 1655.3 cm^{-1} and 1657.3 cm^{-1})

Central Frequency of Doublet (cm^{-1})	Upper State (ν_1 ν_3 ν_3)-(N' K_a' K_c')						Lower State (ν_1 ν_3 ν_3)-(N'' K_a'' K_c'')					
1655.315	(0	0	1)-(58	1	58)	(0	0	0)-(57	1	57)		
1655.456	(0	0	1)-(57	1	56)	(0	0	0)-(56	1	55)		
1655.563	(0	0	1)-(57	2	55)	(0	0	0)-(56	2	54)		
1655.894	(0	0	1)-(59	0	59)	(0	0	0)-(58	0	58)		
1656.301	(0	0	1)-(60	1	60)	(0	0	0)-(59	1	59)		
1656.410	(0	0	1)-(59	1	58)	(0	0	0)-(58	1	57)		
1656.596	(0	0	1)-(59	2	57)	(0	0	0)-(58	2	56)		

Simulated H₂O and NO₂ Spectra —NO2 —H2O
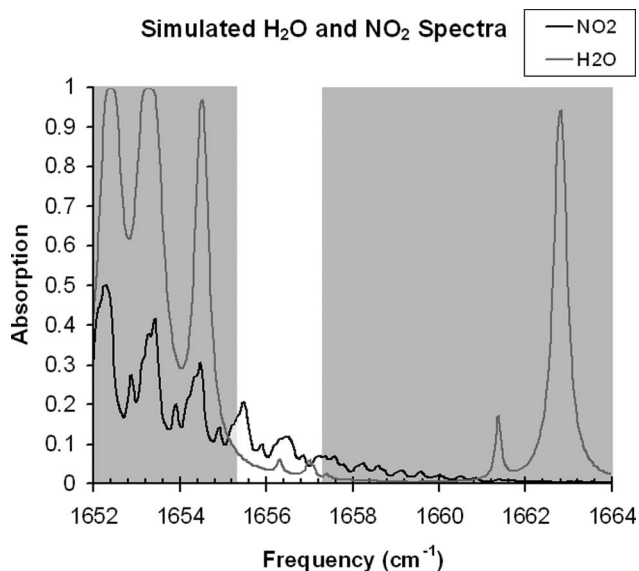
Fig. 3. Simulated H_2O and NO_2 spectra (at 1000 mbars) in the range $1652 \, cm^{-1}$ to $1664 \, cm^{-1}$. To facilitate seeing the weak NO_2 lines in this region and comparing their positions to that of the H_2O lines, a simulated NO_2 concentration of 5 ppm and a path length of 1000 m were used (this path length is of the order of the effective path length of the CRD cell used in reported work). The H_2O spectrum was generated to match typical conditions in the midlatitude United States during the winter months (the time period during which the reported data were recorded) over a 1 m path (corresponding to the path length from the QCL to the CRD cell). This spectrum was used to select a region with a dense NO_2 spectrum that was free from interference due to water lines. The region used for the reported work (between $1655.3 \, cm^{-1}$ and $1657.3 \, cm^{-1}$) is highlighted in the chart with a white background.

where the water lines (due to ambient water vapor in the beam path leading to the experimental cell) overlap and thus overwhelm any potential NO_2 signal in the target region. Because of the broad width and tails of these water lines, our ability to record relatively weak NO_2 spectra was limited to the region between 1655 and $1660 \, cm^{-1}$. As mentioned earlier, the PZT tuning characteristics of the laser limited our tuning range to $2 \, cm^{-1}$; thus, we proceeded with selecting a $2 \, cm^{-1}$ region within this range. The 1655.3 and $1657.3 \, cm^{-1}$ region was selected, because it was far enough from the strong water line at $1654.5 \, cm^{-1}$ [due to the transition between the $(0 \ 1 \ 0)$-$(5 \ 2 \ 3)$ and $(0 \ 0 \ 0)$-$(5 \ 1 \ 4)$ levels] to avoid interference, yet included NO_2 lines that were not too weak [23]. The two water lines that were in the target region [located at 1656.3 and $1657.1 \, cm^{-1}$, due to the transitions between the $(0 \ 1 \ 0)$-$(6 \ 4 \ 3)$ and $(0 \ 0 \ 0)$-$(5 \ 5 \ 0)$ levels and the $(0 \ 1 \ 0)$-$(6 \ 4 \ 2)$ and $(0 \ 0 \ 0)$-$(5 \ 5 \ 1)$ levels, respectively] were weak enough that they did not overwhelm the NO_2 signal. Additionally, since the water vapor in the beam path leading to the experimental cell remained constant for all NO_2 concentrations used, the effects of these water lines were subtracted from the recorded NO_2 signal (as part of the 0 ppm background measurement discussed in Section 5).

We have not directly accounted for water vapor continuum absorption effects. However, it should be stated that the line positions and line intensities calculated using the HITRAN data agreed well with the experimental results. The strength of the water lines was selected to match typical conditions in the midlatitude United States during the winter months (the water vapor density used was $3.46 \, g/m^3$, which corresponds to a relative humidity of 68% at $1 \, °C$, and is the average relative humidity in Washington, D.C. in January) [28]. The strength and width of the water lines in the simulation were calibrated to match our experimental apparatus (which had a roughly 1 m path from the laser to the experimental cell).

It is important to note that the reported work used mixtures of NO_2 with zero air (a dehumidified, simulated air mixture); thus, the steps to avoid the effects of water lines described above pertain only to water vapor present in the beam path leading to the experimental cell. A complication that would need to be addressed before developing this into a field-deployable instrument therefore would be the interference due to water vapor in atmospheric NO_2 samples. Ambient air samples would contain high enough levels of water vapor such that the water lines in the region around the NO_2 lines would completely mask any NO_2 signature (i.e., the water lines are strong enough to result in 100% absorption over the path lengths typical for an ICOS-based apparatus). As a result, dehumidification would need to be performed on samples prior to measurement. Eliminating water vapor in the atmospheric air sample without changing the concentration of highly reactive NO_2 present in traces can be a major challenge, and this is likely to involve elaborate experimentation.

To maximize the integrated signal, the NO_2 concentrations were maintained at a pressure of $1000 \pm 100 \, mbars$. Data from 128 scans were averaged using the on-board memory of a Tektronix DPO3034 digitizing oscilloscope. The oscilloscope output was fed to a PC via USB connection and recorded using Tektronix software.

It is important to note that, in this demonstration of the technique, there was a potential complication introduced by integrating over a fraction of the R band: integrating over the tail of the band could make the strength of the observed lines dependent on the sample's temperature and pressure. As previously mentioned, however, the samples were maintained at a constant pressure of one atmosphere. In order to minimize the adsorption of NO_2 onto the cell walls and CRD mirrors, the apparatus was heated and maintained at a constant temperature of approximately $40 \, °C$. As a result, the amplitude of the NO_2 absorption spectra over the target region (and thus the integrated signal strength as measured by this apparatus) should vary only as a function of NO_2 concentration.

5. Results and Discussion

Absorption spectra were recorded for several concentrations of NO_2: 1900 ppb, 1350 ppb, 1000 ppb, 750 ppb, 500 ppb, 250 ppb, and 0 ppb. By recording the spectra for the weaker lines in the 1655.3 cm⁻¹ and 1657.3 cm⁻¹ region, the effective concentrations of these mixtures were 11.9 ppb, 8.4 ppb, 6.3 ppb, 4.7 ppb, 3.1 ppb, 1.6 ppb, and 0 ppb. The 0 ppb spectrum was recorded to determine the noise contributions from all components of the experiment as well as the contributions from the tails of the water lines in the region of interest (due to water vapor in the beam path) and was generated by filling the sample cell with zero air.

The data from each spectrum were integrated to yield the total absorption strength S_T for the corresponding concentration. Each of these values was subtracted from the total absorption strength recorded for the 0 ppm concentration; this results in the area under the recorded absorption spectrum for the corresponding concentration (we refer to this as the total absorption signal for a given concentration). Figure 4(a) shows a plot of the total absorption signal versus concentration, as well as a weighted linear least-squares fit of these data (the y axis is given in arbitrary units). Figure 4(b) uses an expanded scale to display the low-concentration portion of the data.

The instrument's sensitivity was calculated by determining the noise level in the integrated absorption signal. This was accomplished by repeatedly filling the cell with zero air, recording the corresponding absorption spectra, determining the integrated absorption signal from these spectra, and calculating the standard deviation of these measurements. The standard deviation was then compared to the integrated absorption signals recorded for different concentrations of NO_2. Specifically, we loaded the CRD cell with 1 atm of zero-air 23 times and recorded the corresponding integrated absorption signal (the recorded signal for each data set was an average of 128 scans). The standard deviation of the integrated absorption signal was found to be 0.18%, which corresponded to approximately 50.9 total absorption units. The minimum detectable concentration (at the 1σ level) is found by dividing the standard deviation of 50.9 total absorption units by the slope of the weighted linear least-squares fit of the data recorded from the NO_2 concentrations (1841 total absorption units/ppb). The slope was used since it incorporated uncertainties from all aspects of the apparatus (e.g., the repeated use of the apparatus with several different concentrations of NO_2). The standard deviation in the value of the slope from the weighted least-squares fit was 2.9%. Using these data, we determined the sensitivity of the apparatus to be approximately 28 ppt.

It should be noted that we were limited to the number of data sets mentioned above due to the relatively large volume of our vacuum system, gas mixing apparatus, and experimental cells (~4 liters). The
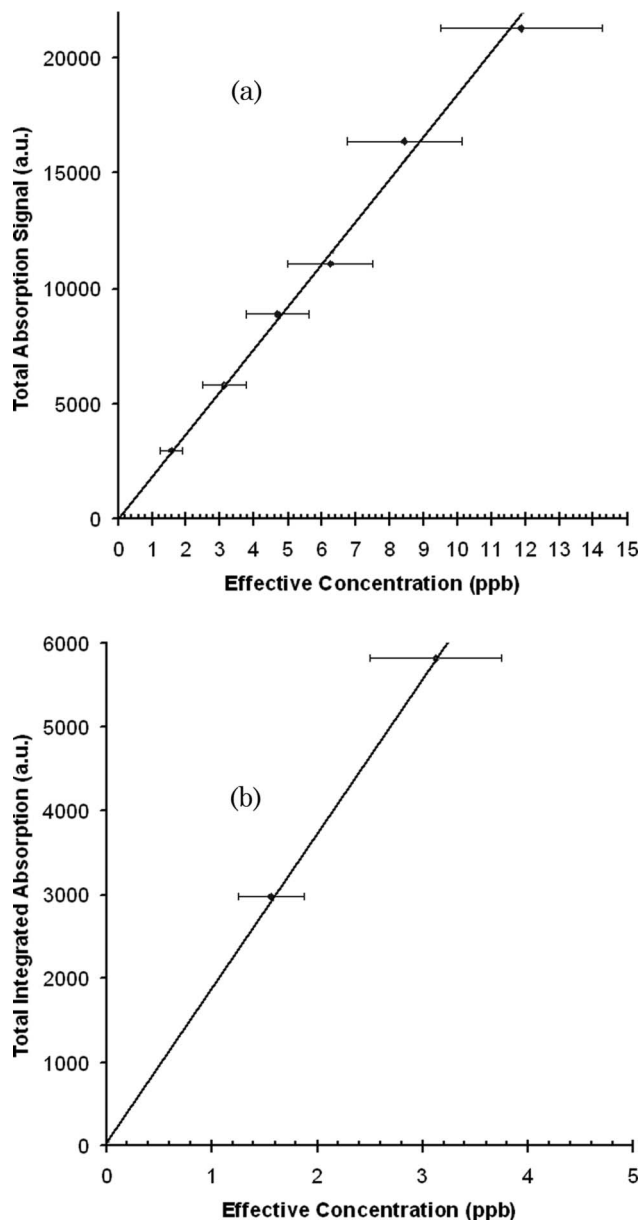
Fig. 4. (a) Total integrated absorption signal versus concentration plot. The expected linear relationship between the multiple-line integrated absorption signals versus concentrations is clearly seen. (b) An expanded scale of the low-concentration region is employed to clearly display the low-concentration data points.

103 liter cylinders of zero air used could typically fill the apparatus 25 to 30 times before their contents were exhausted. Changing cylinders exposed a small section of the apparatus to ambient air. This exposure required us to pump on the system for a few hours before continuing with experiments. A new gas mixing system is currently being designed and should alleviate this problem in the future.

These results show an improvement of approximately 4 orders of magnitude over the previous work where we have employed simple MLIAS (no cavity enhancement) using a short cell of 12.5 cm length and a total path length of 0.88 m and reported a sensitivity of detection of 120 ppb [16]. This magnitude

of improvement is as expected. Specifically, the use of ICOS increases the effective path length by over 3 orders of magnitude over the 88 cm path length used previously. An additional order of magnitude improvement was expected by averaging 128 scans per concentration and from reduced uncertainty in the mixed NO_2 concentrations through improvements to the gas mixing apparatus. These results are among the most sensitive measurements of NO_2 to date. Other recent highly sensitive measurements of NO_2 include the work by Taketani *et al.* [29] that achieved 0.14 parts per billion by volume (ppbv) sensitivity using laser-induced fluorescence and a diode-pumped YAG laser and Zahniser *et al.* [30], who used a continuous wave QCL operating at room temperature and a 210 m multipass cell to report a trace gas detection limit of 1 ppt and ambient measurements of NO_2 with detection precision of 10 ppt $Hz^{-1/2}$. It is important to note that, because the MLIAS technique requires integrating over several absorption features, the selectivity is less compared with the selectivity one can achieve with low-pressure measurements employing the amplitude of a single line absorption feature particularly for molecules with well-resolved spectra. This can be a problem if high-concentration species in the atmosphere such as water vapor have even the tails of their absorption features in the region chosen. However, in cases of molecules with congested spectra and when measurements have to be performed at high pressures, as well as in cases when the absorption features are not well resolved, the MLIAS technique is an excellent choice for high sensitivity of detection. Additionally, the use of ICOS makes the apparatus less susceptible to vibrations compared with other long-path techniques such as CRDS and multipass cells.

6. Conclusion

We demonstrate a highly sensitive sensor for trace gas detection by using MLIAS and enhancing the effective path length by using integrated cavity output spectroscopy. This combination of techniques allowed the detection of trace concentrations of NO_2 with a high sensitivity of the order of 28 ppt. We feel that this technique will be useful for the detection of other polyatomic species besides NO_2 that have dense rotational–vibrational spectra over a relatively compact frequency range. Though this experiment was conducted using a QCL with a wide mode-hop free tuning range, it could be applied using any tunable laser source, such as a diode laser capable of tuning across multiple transitions of the target species.

References

1. "Primary national ambient air quality standards for nitrogen dioxide; final rule," Federal Register **75**(26), 6474–6537 (9 February 2010).
2. United States Environmental Protection Agency, "National air quality status and trends through 2007," EPA-454/R-08-006 (United States Environmental Protection Agency, 2008).
3. J. Hildenbrand, J. Herbst, J. Wöllenstein, and A. Lambrecht, "Explosive detection using infrared laser spectroscopy," Proc. SPIE **7222**, 72220B (2009).
4. T. H. Risby and S. F. Solga, "Current status of clinical breath analysis," Appl. Phys. B **85**, 421–426 (2006).
5. G. M. Mitchell, V. Vorsa, G. L. Ryals, J. A. Milanowicz, D. J. Ragsdale, K. L. Marhefka, and S. N. Ketkar, "Trace impurity detection in ammonia for the compound semiconductor market," presented at the SEMI Technical Symposium: Innovations in Semiconductor Manufacturing, Semicon West, San Francisco, California, USA (17–21 July 2002).
6. A. Arnold, H. Becker, R. Hemberger, W. Hentschel, W. Ketterle, M. Kollner, W. Meienburg, P. Monkhouse, H. Neckel, M. Schafer, K. P. Schindler, V. Sick, R. Suntz, and J. Wolfrum, "Laser *in situ* monitoring of combustion processes," Appl. Opt. **29**, 4860–4872 (1990).
7. A. A. Kosterev, R. F. Curl, F. K. Tittel, M. Rochat, M. Beck, D. Hofstetter, and J. Faist, "Chemical sensing with pulsed QC-DFB lasers operating at $6.6 \mu m$," Appl. Phys. B **75**, 351–357 (2002).
8. F. K. Tittel, Y. Bakhirkin, A. Kosterev, and G. Wysocki, "Recent advances in trace gas detection using quantum and interband cascade lasers," Rev. Laser Eng. **34**, 275–282 (2006).
9. R. F. Curl, F. Capasso, C. Gmachl, A. A. Kosterev, B. McManus, R. Lewicki, M. Pusharsky, G. Wysocki, and F. K. Tittel, "Quantum cascade lasers in chemical physics," Chem. Phys. Lett. **487**, 1–18 (2010).
10. G. N. Rao and A. Karpf, "External cavity tunable quantum cascade lasers and their applications to trace gas monitoring," Appl. Opt. **50**, A100–A115 (2011).
11. A. O'Keefe, J. J. Scherer, and J. B. Paul, "CW integrated cavity output spectroscopy," Chem. Phys. Lett. **307**, 343–349 (1999).
12. R. Engeln, G. Berden, R. Peters, and G. Meijer, "Cavity enhanced absorption and cavity enhanced magnetic rotation spectroscopy," Rev. Sci. Instrum. **69**, 3763–3769 (1998).
13. J. B. Paul, L. Lapson, and J. G. Anderson, "Ultrasensitive absorption spectroscopy with a high-finesse optical cavity and off-axis alignment," Appl. Opt. **40**, 4904–4910 (2001).
14. G. Berden, R. Peeters, and G. Meijer, "Cavity ring-down spectroscopy: experimental schemes and applications," Int. Rev. Phys. Chem. **19**, 565–607 (2000).
15. G. N. Rao and A. Karpf, "High sensitivity detection of NO_2 employing cavity ring-down spectroscopy and an external cavity continuously tunable quantum cascade laser," Appl. Opt. **49**, 4906–4914 (2010).
16. A. Karpf and G. N. Rao, "Enhanced sensitivity for the detection of trace gases using multiple line integrated absorption spectroscopy," Appl. Opt. **48**, 5061–5066 (2009).
17. A. Karpf and G. N. Rao, "Enhancement of trace gas detection by integrating wavelength modulated spectra across multiple lines," Appl. Opt. **49**, 1406–1413 (2010).
18. J. H. Van Helden, R. Peverall, and G. A. D. Ritchie, "Cavity enhanced techniques using continuous wave lasers," in *Cavity Ring-Down Spectroscopy*, G. Berden and R. Engeln, eds. (Wiley, 2009), pp. 27–56.
19. Y. A. Bakhirkin, A. A. Kosterev, R. F. Curl, F. K. Tittel, D. A. Yarekha, L. Hvozdara, M. Giovannini, and F. Faist, "Sub-ppbv nitric oxide concentration measurements using CW thermoelectrically cooled quantum cascade laser-based integrated cavity output spectroscopy," Appl. Phys. B **82**, 149–154 (2006).
20. M. L. Silva, D. M. Sonnenfroh, D. I. Rosen, M. G. Allen, and A. O'Keefe, "Integrated cavity output spectroscopy measurements of nitric oxide levels in breath with a pulsed room-temperature quantum cascade laser," Appl. Phys. B **81**, 705–710 (2005).

21. K. W. Busch, A. Hennequin, and M. A. Busch, "Introduction to optical cavities," in *Cavity Ringdown Spectroscopy*, K. W. Busch and M. A. Busch, eds. (American Chemical Society, 1999), pp. 20–33.

22. J. M. Hollas, *High Resolution Spectroscopy*, 2nd ed. (Wiley, 1998).

23. L. S. Rothman, D. Jacquemart, A. Barbe, D. C. Benner, M. Birk, L. R. Brown, M. R. Carleer, C. Chackerian, Jr., K. Chance, L. H. Coudert, V. Dana, V. M. Devi, J.-M. Flaud, R. R. Gamache, A. Goldman, J.-M. Hartmann, K. W. Jucks, A. G. Maki, J.-Y. Mandin, S. T. Massie, J. Orphal, A. Perrin, C. P. Rinsland, M. A. H. Smith, J. Tennyson, R. N. Tolchenov, R. A. Toth, J. Vander Auwera, P. Varanasi, and G. Wagner, "The HITRAN 2004 molecular spectroscopic database," J. Quant. Spectrosc. Radiat. Transfer **96**, 139–204 (2005).

24. C. N. Mikhailenko, Y. L. Babikov, and V. F. Golovko, "Information-calculating system spectroscopy of atmospheric gases: the structure and main functions," Atmos. Ocean. Opt. **18**, 685–695 (2005).

25. National Aeronautic and Space Administration, "Earth fact sheet—terrestrial atmosphere," http://nssdc.gsfc.nasa.gov/planetary/factsheet/earthfact.html.

26. E. De Tommasi, G. Casa, and L. Gianfrani, "High precision determinations of NH_3 concentration by means of diode laser spectrometry at $2.005\,\mu m$," Appl. Phys. B **85**, 257–263 (2006).

27. E. Burkhard and J. Schwab, "Ambient gaseous ammonia: evaluation of continuous measurement methods suitable for routine deployment—final report," (New York State Energy Research and Development Authority, 2008).

28. National Oceanic and Atmospheric Administration, "Average relative humidity," http://lwf.ncdc.noaa.gov/oa/climate/online/ccd/avgrh.html.

29. F. Taketani, M. Kawai, K. Takahashi, and Y. Matsumi, "Trace detection of atmospheric NO_2 by laser-induced fluorescence using a GaN diode laser and a diode-pumped YAG laser," Appl. Opt. **46**, 907–915 (2007).

30. M. Zahniser, D. Nelson, J. McManus, S. Herndon, E. Wood, J. Shorter, B. Lee, G. Santoni, R. Jiménez, B. Daube, S. Park, E. Kort, and S. Wofsy, "Infrared QC laser applications to field measurements of atmospheric trace gas sources and sinks in environmental research: enhanced capabilities using continuous wave QCLs," Proc. SPIE **7222**, 72220H (2009).